MINIMIZING THE AVERAGE AXIS DRIFT OF DOUBLE CROSS-AXIS FLEXURAL PIVOTS

RUIYU BAI, GUIMIN CHEN*

Abstract. A compliant revolute joint achieves its rotational DOF through the deflections of its flexible members, thus completely eliminates clearance and friction between connected parts. Various compliant revolute joints have been created using notch and leaf spring primitives, including but not limited to cross-axis flexural pivots, cartwheel flexures, and trapezoidal flexures. Although compliant joints offer superior operating characteristics, most of them undergo imprecise motion referred to as axis drift. By using the analog of the design of double parallel-guided mechanism for translation shift elimination, this work proposes a double cross-axis flexural pivot that connects two cross-axis flexural pivots to eliminate the axis drifts by each other. A kinetostatic model is developed, based on which a double cross-axis flexural pivot is modeled. Axis drift of the double cross-axis flexural pivot with different connection angles are discussed. The optimal connection angles for different rotation ranges are obtained. The design results are verified by those of a nonlinear finite element model.

Key words: Cross-axis flexural pivot, double cross-axis flexural pivot, chained beam constraint model, axis drift.

1. INTRODUCTION

A compliant revolute joint achieves its rotational DOF through the deflections of its flexible members, thus completely eliminating the clearance and friction between connected parts [1], [2]. As a result, the compliant revolute joint has been widely used in various fields, such as large stroke flexure mechanisms [3], compliant linear motion mechanisms [4], precision positioning stages [5], actuators [6] and aerospace mechanisms [7], etc. Various compliant revolute joints have been created using notch and leaf spring primitives, including but not limited to cross-axis flexure pivot [4, 8-10], cartwheel flexure [11], trapezoidal flexures [12] and butterfly pivots [13]. Although compliant joints offer superior operating characteristics, only a limited angular range can be achieved due to the permissible stress and strain in the material (All flexures are limited to a finite range of motion, while their rigid counterparts rotate infinitely). In addition to a limited range of motion, most compliant joints undergo imprecise motion referred to as axis drift,

School of Mechanical Engineering, Xi’an Jiaotong University, Xi’an, Shannxi 710049, China
*Corresponding author: guimin.chen@xjtu.edu.cn

Ro. J. Techn. Sci. − Appl. Mechanics, Vol. 67, N° 1, P. 23–41, Bucharest, 2022

the center of rotation does not remain fixed with respect to the links it connects and can considerably deviate from the axis of straight-line motion.

Among various compliant joints, the cross-axis flexural pivot (CAFP) is a compact bearing ideally suited for angular deflection (rotation) of up to 30 degrees [14]. However, the axis of rotation of a CAFP considerably shifts when moved through the range of angular motion, which can be detrimental in precision applications. The axis shift is defined as the difference between the diameter centers of the moved portion of the pivot and the portion (or portions) that are fixed (axial drift factor). In general, the axis shift can be divided into two parts, one is the kinematic part (will be referred to as the axis drift) and the other is the shift due to radial loads [15]. The axis shift caused by radial loads can be characterized by the radial stiffness of the joint, while the axis shift produced when only a pure moment is applied (which will be referred to as the axis drift in the following) is an intrinsic kinematic characteristic that occurs as a function of the deflected angle.

To facilitate the application of CAFP, several methods for modelling and design of flexures, such as the pseudo-rigid body method [15-17], the comprehensive elliptic integral solution [18-19], the beam constraint model (BCM) [20] and chained beam constraint model (CBCM) [21], [22], the screw theory [23] and the FACT [24], [25], are employed to obtaining the accuracy characteristics of it. Since the CBCM has the advantages of high accuracy in modeling large deflections of flexures and simplicity in mathematics, it is employed to model the CAFPs proposed in this work.

The double cross-axis flexural pivot (DCAPF) connects two identical joints in series with their centers of rotation collocated has been proposed to mitigate the axis drift [14]. Analogy to the folded parallel-guiding compliant mechanism (translational joint) shown in Fig. 1, the axis drifts of the two CAFPs can be compensated by each other. However, the DCAFPs haven not been modeled precisely, and the axis drift properties have not been discussed in detail. In this work, we firstly model the CAFP by using the CBCM and obtained the accurate axis drift of it. Then the axis drift of the DCAFP, in which the two cross-axis flexural pivot are connected with a certain angle, is derived based on the axis drift of CAFP. Further, by optimizing the connection angles of the two CAFPs in DCAFP, the optimal connection angles to address the minimum average axis drift in a certain rotation range are obtained.

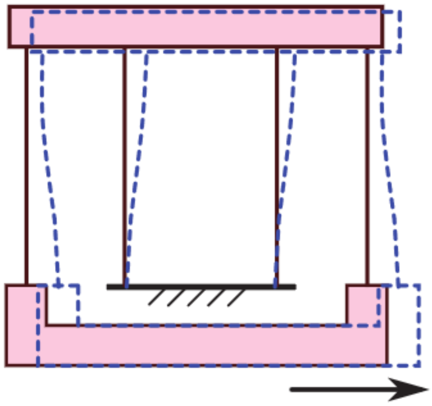

Fig. 1 – Folded parallel-guiding compliant mechanism.

The rest of this paper is organized as follows: The modeling of a CAFP by employing the CBCM is represented in Sec.2 and the axis drift of the CAFP is also shown in this section. In Sec.3, the expressions of axis drift in DCAFP are deduced based on the axis drift of CAFP. The minimizing of the average axis drift of the DCAFP with a certain rotation range is also done in this section. Concluding remarks and future works are included in Sec.4.

2. MODELING CROSS-AXIS FLEXURAL PIVOT

As shown in Fig. 2, a cross-axis flexural pivot contains two identical beam flexures (beam O_1B and beam O_2A) with length L, width W and thickness T and two rigid part O_1O_2 and AB. The rigid part O_1O_2 is the fixed end and the rigid part AB is the moving part. Midpoint of O_1O_2 and AB are defined as O and C, respectively. A global coordinate frame (xOy) is established on the point O with its x-axis point from O to O_2 and the y-axis point from O to C before deflection. In the global frame, two beam flexures in the CAFP are oriented symmetrically about the y-axis. The angle between the two beams is 2β. Let $L_{O_1O_2} = w_1$, $L_{AB} = w_2$ and $N_o = w_1 / w_2$, we have

$$\begin{cases} w_1 = \dfrac{2N_oL}{1+N_o}\sin\beta, \\ w_2 = \dfrac{2L}{1+N_o}\sin\beta. \end{cases} \tag{1}$$

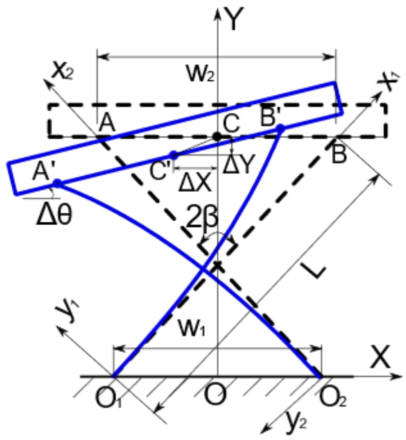

Fig. 2 – Geometry of cross-axis flexural pivot.

By applying external planar loads on the center point of the moving stage (point C), deflections of the moving stage can be represented by the translational displacements of point C along x and y directions (ΔX and ΔY) and the in-plane rotation displacement ($\Delta\theta$). According to the displacement of point C, displacement components of the moving ends of the beam flexures in the xOy frame are obtained as

$$\begin{cases} U_{xA} = \Delta X + \dfrac{w_2}{2}\cos\Delta\theta, \\ U_{yA} = \Delta Y - \dfrac{w_2}{2}\sin\Delta\theta, \\ U_{xB} = \Delta X - \dfrac{w_2}{2}\cos\Delta\theta, \\ U_{yB} = \Delta Y + \dfrac{w_2}{2}\sin\Delta\theta, \\ \theta_A = \theta_B = \Delta\theta. \end{cases} \tag{2}$$

In order to model the deflections of the beam flexures in the CAFP, local coordinate frames $x_1O_1y_1$ and $x_2O_2y_2$ are established at point O_1 and O_2, respectively. The x_1-axis along the length direction of O_1B before deflection and y_1-axis is perpendicular to x_1-axis and follows the right-hand rule. Similarly, the x_2-axis along the length direction of O_2A before deflection and y_2-axis perpendicular to x_2-axis and follows the right-hand rule. In terms of the coordinate transformation, displacement components of the beam flexures in the corresponding local coordinate frames are

$$\begin{aligned}
\begin{Bmatrix} \bar{U}_{xA} \\ \bar{U}_{yA} \end{Bmatrix} &= \begin{bmatrix} \cos\left(\frac{\pi}{2}+\beta\right) & \sin\left(\frac{\pi}{2}+\beta\right) \\ -\sin\left(\frac{\pi}{2}+\beta\right) & \cos\left(\frac{\pi}{2}+\beta\right) \end{bmatrix} \begin{Bmatrix} U_{xA} \\ U_{yA} \end{Bmatrix}, \\
\begin{Bmatrix} \bar{U}_{xB} \\ \bar{U}_{yB} \end{Bmatrix} &= \begin{bmatrix} \cos\left(\frac{\pi}{2}-\beta\right) & \sin\left(\frac{\pi}{2}-\beta\right) \\ -\sin\left(\frac{\pi}{2}-\beta\right) & \cos\left(\frac{\pi}{2}-\beta\right) \end{bmatrix} \begin{Bmatrix} U_{xB} \\ U_{yB} \end{Bmatrix}.
\end{aligned} \tag{3}$$

By utilizing the same normalization method as in [20], the normalized displacements of the beams are obtained as

$$\begin{cases}
\bar{u}_{xa} = \dfrac{\bar{U}_{xA}}{L}, \\
\bar{u}_{ya} = \dfrac{\bar{U}_{yA}}{L}, \\
\bar{\theta}_a = \Delta\theta, \\
\bar{u}_{xb} = \dfrac{\bar{U}_{xB}}{L}, \\
\bar{u}_{yb} = \dfrac{\bar{U}_{yB}}{L}, \\
\bar{\theta}_b = \Delta\theta.
\end{cases} \tag{4}$$

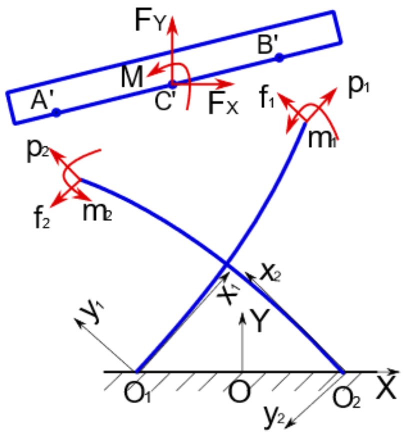

Fig. 3 – Free-body diagrams of cross-axis flexural pivot.

As shown in Fig. 3, the loads applied to the beam O_1B are p_1, f_1 and m_1, in which, p_1 is the normalized axial force, f_1 is the normalized lateral force and m_1 is the normalized bending moment. Similarly, the loads on the beam O_2A are p_2, f_2 and m_2. The external loads applied on point C are F_x, F_y and M. For the load equilibrium, the external loads and internal loads follow the relationships as

$$\begin{cases} \dfrac{F_x L^2}{EI} = p_1 \cos\left(\dfrac{\pi}{2}-\beta\right) - f_1 \sin\left(\dfrac{\pi}{2}-\beta\right) + \\ \qquad + p_2 \cos\left(\dfrac{\pi}{2}+\beta\right) - f_2 \sin\left(\dfrac{\pi}{2}+\beta\right), \\ \dfrac{F_y L^2}{EI} = p_1 \sin\left(\dfrac{\pi}{2}-\beta\right) + f_1 \cos\left(\dfrac{\pi}{2}-\beta\right) + \\ \qquad + p_2 \sin\left(\dfrac{\pi}{2}+\beta\right) + f_2 \cos\left(\dfrac{\pi}{2}+\beta\right), \\ \dfrac{ML}{EI} = m_1 + m_2 + \left(p_1 \sin\left(\dfrac{\pi}{2}-\beta\right) + f_1 \cos\left(\dfrac{\pi}{2}-\beta\right)\right)\dfrac{X_B - X_C}{L} - \\ \qquad - \left(p_1 \cos\left(\dfrac{\pi}{2}-\beta\right) - f_1 \sin\left(\dfrac{\pi}{2}-\beta\right)\right)\dfrac{Y_B - Y_C}{L} + \\ \qquad + \left(p_2 \sin\left(\dfrac{\pi}{2}+\beta\right) + f_2 \cos\left(\dfrac{\pi}{2}+\beta\right)\right)\dfrac{X_A - X_C}{L} - \\ \qquad - \left(p_2 \cos\left(\dfrac{\pi}{2}+\beta\right) - f_2 \sin\left(\dfrac{\pi}{2}+\beta\right)\right)\dfrac{Y_A - Y_C}{L}, \end{cases} \tag{5}$$

in which E is the Young's modulus of material and I is the second moment of area of the beam flexures, X_A, Y_A, X_B, Y_B, X_C and Y_C are coordinates of A, B and C in the global frame.

As we have the geometric constraint relations in Eq. (2) and the load equilibrium relations in Eq. (5), the deflections of the CAFP can be obtained by employing the CBCM, which has been deduced in [21] in detail, as the load-displacement relations and giving any three load or displacement components on point C.

All the flexible beams being analyzed in the following parts are made of Polypropylene, with Young's modulus $E = 1.4\times10^9$ Pa and geometric parameters of the CAFP as Table 1 shows. By applying an increasing rotation angle $\Delta\theta$ from 0 to $\pi/2$ and setting the loads components $F_x = F_y = 0$ on point C, the deformed configurations and the reaction moments generated on point C can be obtained by modeling the CAFP by CBCM [21]. For comparison, the pivot was also modeled using the FEA which realized in ANSYS with the beam flexures are meshed into 100 elements using BEAM188, rigid body are modeled by MPC184 element by setting the connection property as "rigid beam" and the geometric nonlinearity option are turned on by using command "NLGEOM, 1".

Table 1

Geometric parametric of the cross-axis flexural pivot

L (m)	W (m)	T (m)	β	N_o
0.05	0.01	0.0006	$\pi/6$	1

Fig. 4 shows the deformed configurations of the CAFP at $\Delta\theta = 0$, $\pi/4$, $\pi/2$, respectively. The solid thinner lines are the deformed beam obtained by CBCM, the "*" lines are the deformed configurations obtained by ANSYS and the thick solid lines represent the rigid parts in CAFP. To show the axis drift clearly, a point O', which coincides with the midpoint of the beam flexures before deflection and is rigidly connected to the rigid part, is also plotted in this figure. One can find that the deformed configurations obtained by CBCM and ANSYS agree well with each other, and there exists an evident axis drift with the increase of $\Delta\theta$. Fog. 5 shows the relationship between the input rotation angles and the corresponding reaction moment on point C. It can be found that the results obtained by CBCM agree well with that obtained by ANSYS, and the load-displacement relation of the cross-axis flexural pivot has a nearly linear relation, i.e., the rotational stiffness is approximated to a constant, which is a good property for the use of the CAFP.

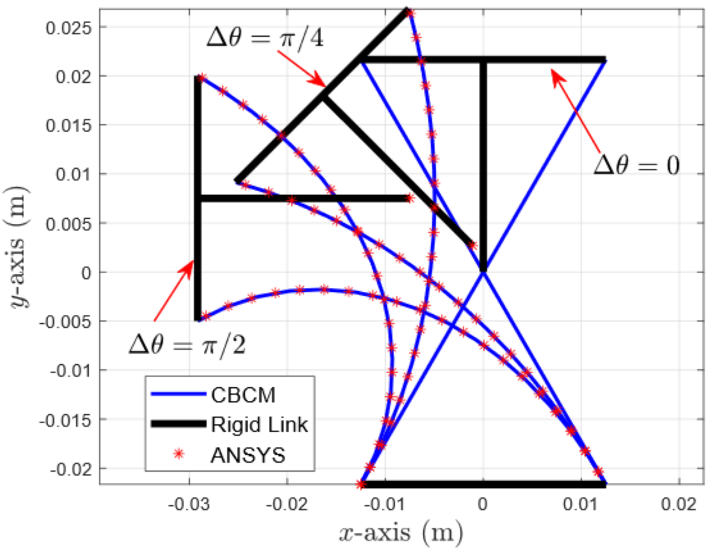

Fig. 4 – Deformed shapes of the CAFP in different rotation angles.

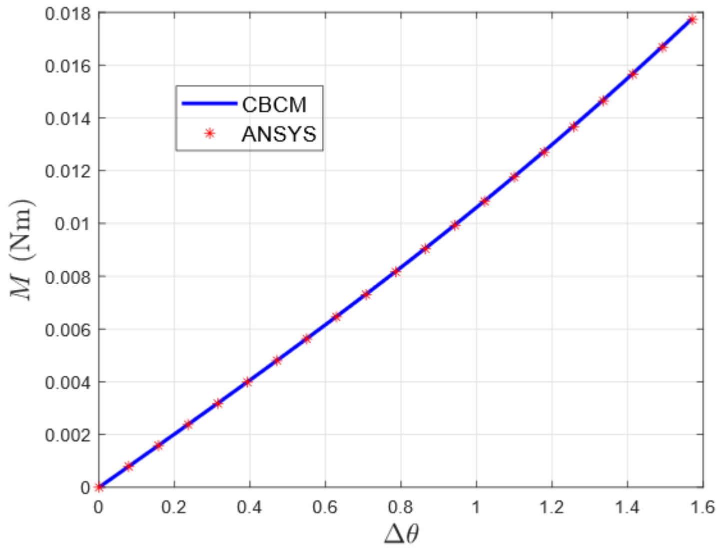

Fig. 5 – Load-displacement relation of the CAFP.

According to the definition of the point O', coordinates of this point at any deformed configuration are

$$\begin{cases} X_{O'} = X_C + \dfrac{L}{2}\cos\beta\sin\Delta\theta, \\ Y_{O'} = Y_C + \dfrac{L}{2}\cos\beta\cos\Delta\theta. \end{cases} \tag{6}$$

Thus, the axis drift D can be obtained as

$$D = \sqrt{\left(X_{O'} - X_{O'_0}\right)^2 + \left(Y_{O'} - Y_{O'_0}\right)^2}\,, \tag{7}$$

where, $X_{O'_0} = 0$ and $Y_{O'_0} = L/2\cos\beta$ are coordinate components of O' before deformation. Giving the rotation angle evenly increase from 0 to $\pi/2$ in 21 steps, the relationship between axis drift D and the rotation angle $\Delta\theta$ is shown in Fig. 6. One can find that the results obtained by CBCM agree well with those obtained by ANSYS. It can be seen that the increase of the rotation angle increases the axis drift sharply.

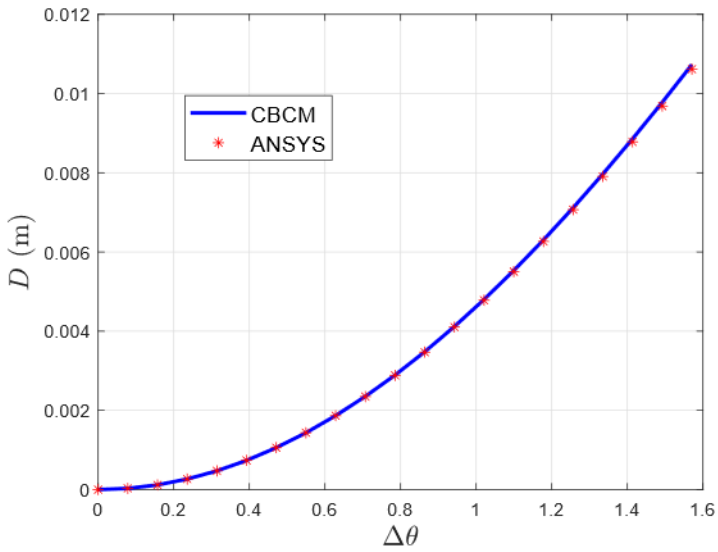

Fig. 6 – Axis drift of the CAFP.

3. MODELING DOUBLE CROSS-AXIS FLEUXRAL PIVOT

Analogous to the double parallelogram flexure, which mitigates the displacement in the degree of constraint directions by series connecting two parallelograms in opposite direction, a double cross-axis pivot is proposed to implement the minimizing of axial drift of the CAFP in this section. Fig. 7 shows a double cross-axis flexural pivot, which can be seen as two cross-axis pivots series connected in opposite direction, comprises three rigid parts and four beam flexures. The rigid part S_1 is the fixed end, the rigid part S_2 is the intermediate stage and the rigid part S_3 is the free end. The two ends of the beam B_1 rigidly connect to S_1 and S_2, respectively, so as to the beam B_2. The two ends of the beam B_3 rigidly connect to S_2 and S_3, respectively, so as to the beam B_4. A coordinate frame with its Z-axis perpendicular to the rotation plane are established. By applying a moment M_z about the Z-axis on S_3, the free end will rotate in the XY plane.

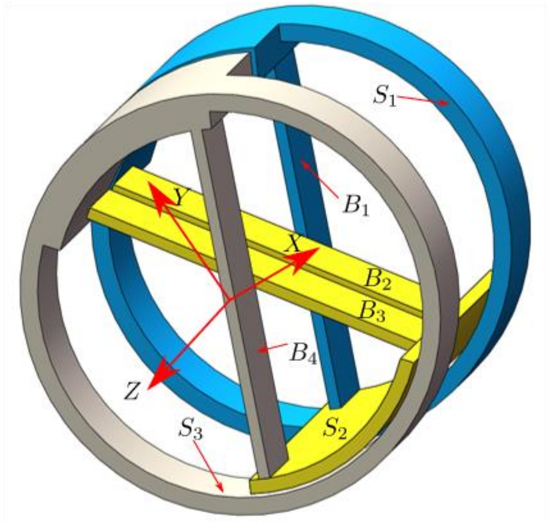

Fig. 7 – Configuration of the DCAFP.

One can find that B_1, B_2, S_1 and S_2 form one CAFP with its fixed end and free end being S_1 and S_2 respectively; this cross-axis pivot is denoted as P_1. Similarly, the other cross-axis pivot comprises B_3, B_4, S_2 and S_3 with its fixed end and free end being S_2 and S_3, respectively, is denoted as P_2. P_1 has the same rotation angle with P_2 when the DCAFP is only subject to a pure external moment M_z on the rigid part S_3. Thus, applying the same moment on the DCAFP and CAFP, the rotation angle α of DCAFP is twice of the rotation angle $\Delta\theta$ of CAFP.

As Fig. 8 shows, for a rotation angle α on the rigid body S_3, the axis drift of P_1 and P_2 are represented by vectors $\vec{d}_1$ and $\vec{d}_2$, respectively. The lengths of the axis drifts are equal, i.e., $\|\vec{d}_1\| = \|\vec{d}_2\|$. Since the "fixed end" of P_2 is S_2, the angle between $\vec{d}_1$ and $\vec{d}_2$ is $\pi - \alpha/2$. The axis drift of the DCAFP is the sum of $\vec{d}_1$ and $\vec{d}_2$, therefore the length of $\vec{d}$ can be calculated as

$$\left\|\vec{d}\right\| = 2\left\|\vec{d}_1\right\| \left|\sin\left(\frac{\alpha}{4}\right)\right| \tag{8}$$

One can find from Eq. (8) that the DCAFP evidently reduces the axis drift compared to the CAFP when α is small. However, with the increase of α, this reduction becomes smaller. When $\alpha = 2\pi/3$, $\left\|\vec{d}\right\| = \left\|\vec{d}_1\right\|$, which means the axis drift of DCAFP at $\alpha = 2\pi/3$ equals the axis drift of CAFP at $\Delta\theta = \pi/3$. Using the same material properties and the geometric parameters as in the example analyzed in Sec. 2, and applying an α increasing from 0 to π, the deformed configurations and the load-displacement relation are shown in Fig. 9 and Fig. 10. One can find that the results obtained by CBCM agree well with those obtained by ANSYS. The relationship between rotation angle and reaction moment is nearly linear. For a certain rotation angle, the moment applied on the DCAFP is half of that applied on the CAFP, which means the DCAFP has larger rotation range and smaller rotational stiffness than the CAFP.

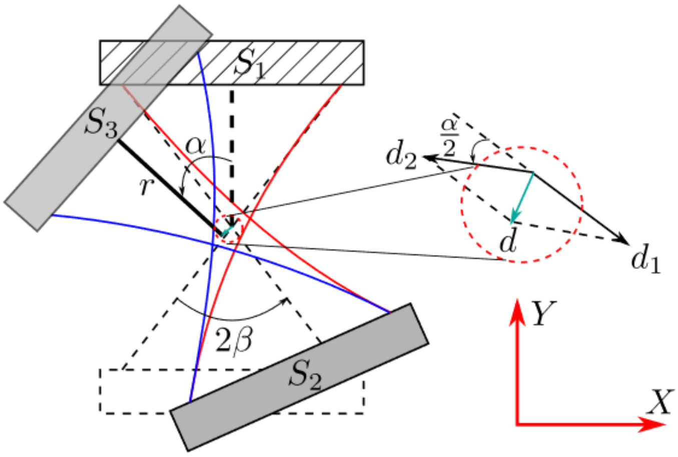

Fig. 8 – Deflection of the DCAFP.

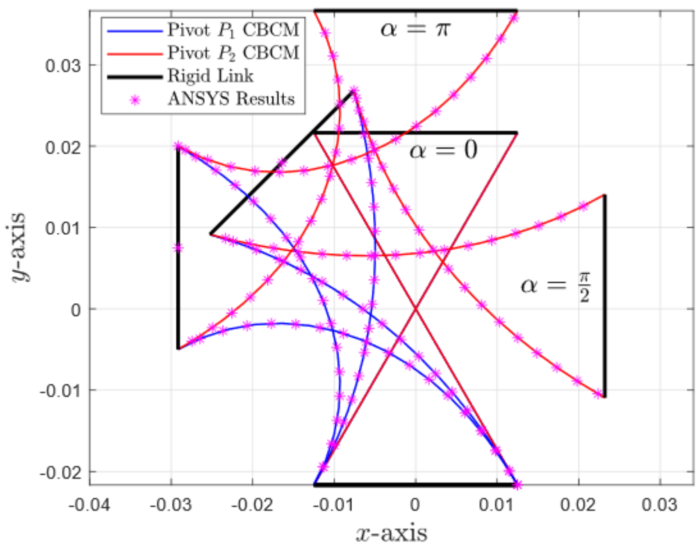

Fig. 9 – Deformed configuration of the DCAFP.

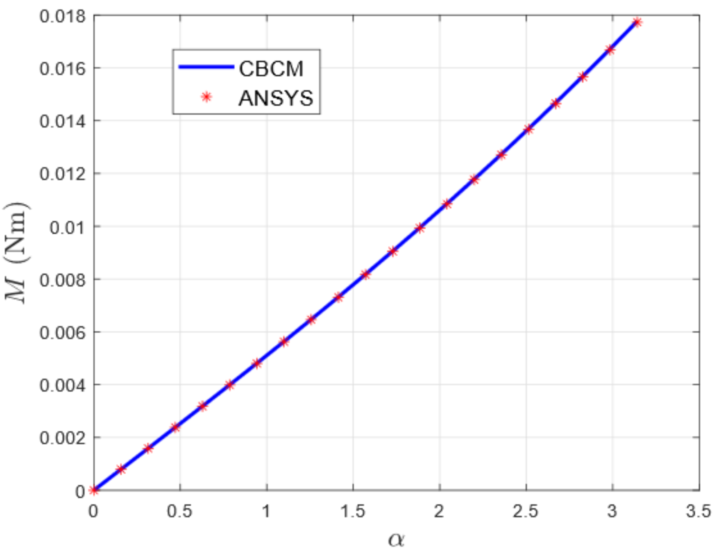

Fig. 10 – Load-displacement relation of the DCAFP.

Taking the axis drift of CAFP obtained in Sec. 2 into Eq. (8), the axis drift of DCAFP can be obtained. Simultaneously, the axis drift can be obtained by modeling the DCAFP in ANSYS. The axis drift obtained by Eq. (8) and ANSYS are plotted in Fig. 11, and the axis drifts of CAFP are also plotted for the performance comparison. One can find that the axis drifts obtained by Eq. (8) agree well with that obtained by ANSYS. The axis drift is very small when α is small, but with the increase of α the axis drift increases sharply. Compared with the CAFP, the DCAFP evidently mitigates the axial drift. However, the DCAFP with the connection angle of π still has a large axial drift when α is large enough.

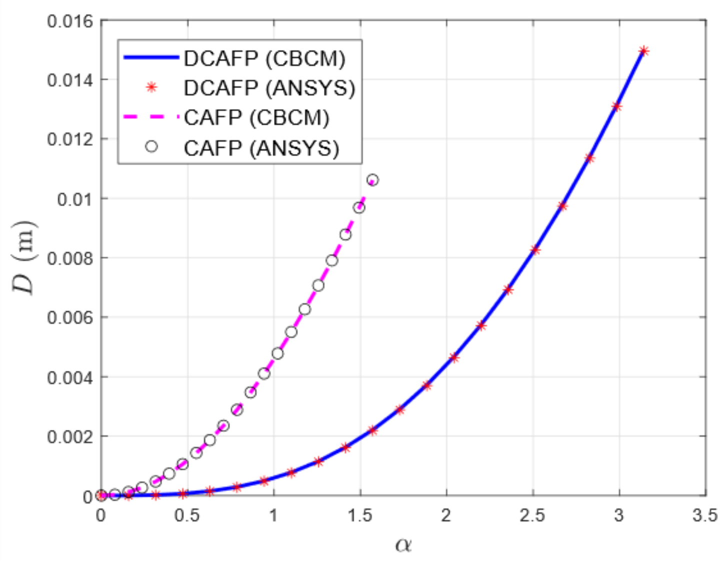

Fig. 11 – Axis drift of the DCAFP.

According to Eq. (8) and Fig. 8, one can find that when P_1 and P_2 are arranged in opposite directions, the length of $\vec{d}$ is increasing and the angle between $\vec{d}_1$ and $\vec{d}_2$ is reducing with the increase of α. For these two reasons, the axis drift increases sharply. Considering the axis drift property of a CAFP is difficult to change, a feasible strategy to minimize the axial drift of DCAFP may be to keep the angle between $\vec{d}_1$ and $\vec{d}_2$ large enough in the assumed rotation range. In other words, to connect the two cross-axis pivots at a certain angle instead of in the opposite direction may facilitate the minimization of the axis drift of DCAFP.

By defining the angle between the two cross-axis flexural pivots as ϕ , the length of $\vec{d}$ can be obtained as

$$\left\|\vec{d}\right\| = 2\left\|\vec{d}_1\right\|\left|\cos\frac{\phi+\frac{\alpha}{2}}{2}\right|. \tag{9}$$

For $\phi, \alpha \in [0, \pi]$, there are two solutions of $\left\|\vec{d}\right\| = 0$, one is $\left\|\vec{d}_1\right\| = 0$, i.e., $\alpha = 0$, the other solution is $\cos\left(\left(\phi + \alpha/2\right)/2\right) = 0$, i.e. $\alpha = 2\left(\pi - \phi\right)$. For instance, when $\phi = \pi/2$ (the configuration of the DCAFP are shown in Fig. 12), the axial drift at $\alpha = 0$ and $\alpha = \pi$ are zero, which means for the rotation range of $[0, \pi]$ the axis drift no longer increases monotonically, but increases at the beginning and then decreases to zero. In this case, the axial drift has evidently decreased when the DCAFP rotates with a large rotation angle. The axis drift of the DCAFP connected with an offset angle $\phi = \pi/2$ is shown in Fig. 13 and one can find that the axis drift has effectively been mitigated by comparing with the opposite connected DCAFP. This gives us a guidance to minimize the axis drift of DCAFP, i.e., by optimizing the connection angle of the two CAFPs we can obtain a minimum average axis drift for a certain rotation range. For instance, the average axis drifts of the DCAFPS which has the rotation range as $[0, \pi]$ in different connection angles are calculated by Eq. (9) and are shown in Figure 14. One can find that the average axis drift has the minimum value when $\phi = 3\pi/5$. Table 2 shows some optimal connection angles for DCAFPs with different rotation ranges. One can find that the optimal connection angle is close to π with the reduction of the rotation range. That is because the connection in opposite direction can get the smallest axis drift in the beginning of the rotation. Besides, one can find that the optimal connection angles for $[0, \pi/2]$ and $[-\pi/2, \pi/2]$ are different because the axis drift is no longer symmetric with respect to $\alpha = 0$ when $\phi \neq \pi$.

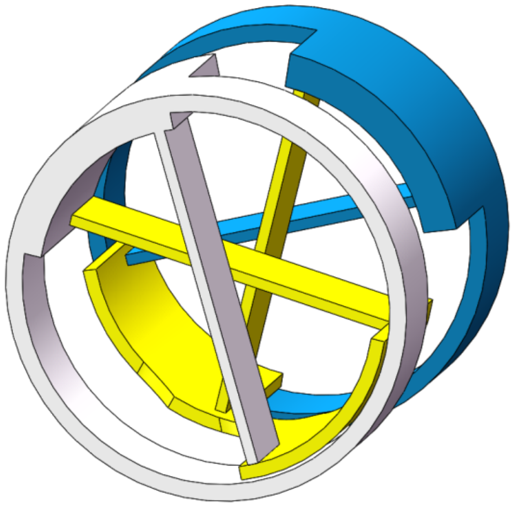

Fig. 12 – Configuration of DCAFP with a general connection angle.

Table 2

The optimal connection angles for DCAFPs with different rotation ranges.

Rotation range	$[0, \pi]$	$[0, 2\pi/3]$	$[0, \pi/2]$	$[-\pi/2, \pi/2]$	$[-\pi/3, 2\pi/3]$
Connection angle	$3\pi/5$	$29\pi/40$	$4\pi/5$	$9\pi/10$	$5\pi/12$

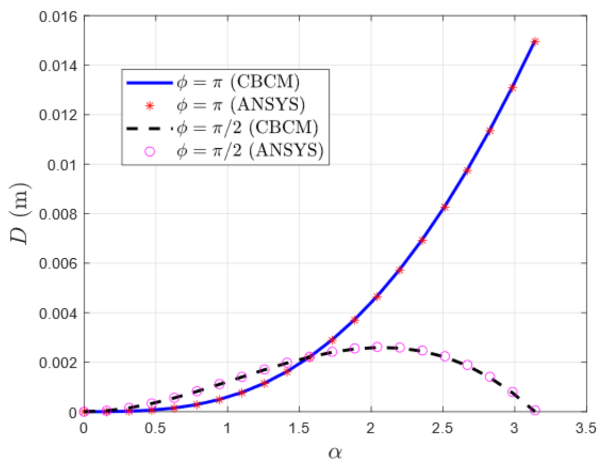

Fig. 13 – Axis drifts of the DCAFP with different connection angles.

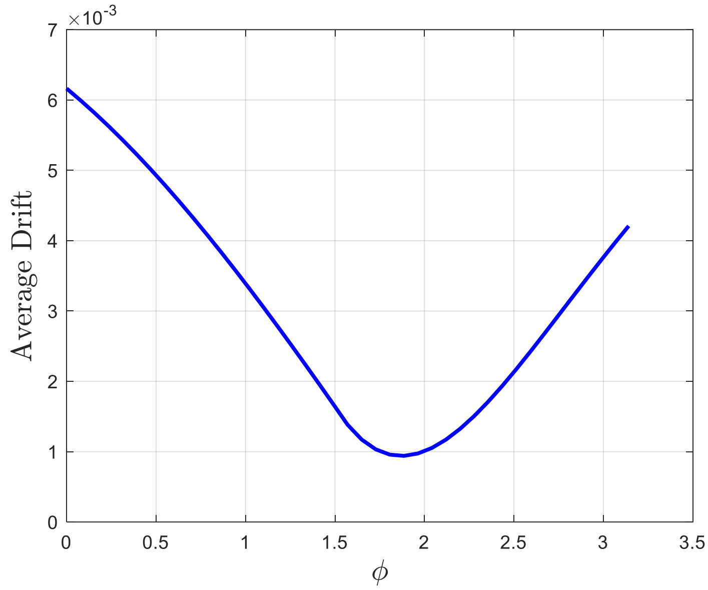

Fig. 14 – Average axis drift of the DCAFP with different connection angles.

4. CONCLUSIONS

In this paper, the double cross-axis flexural pivot (DCAFP) is modeled to increase the rotation range and to minimize the axis drift of the cross-axis flexural pivot (CAFP). By connecting two CAFPs in series, the rotation range of a DCAFP has increased to twice the rotation angles of the corresponding CAFP and the axial drifts result from the two CAFP can partly counteract reciprocally and lead to an evident mitigation of the total axis drift of a DCAFP. The expressions of axis drift for different connection angles of the DCAFP are derived based on the axis drift of CAFP. The optimal connection angles to minimize the average axis drift of the DCAFPs, which have different rotation ranges, are obtained. In future work, a multiple parameters optimization will be introduced to address an optimal design to obtain the minimum axial drift of the DCAFP.

Acknowledgment. The authors gratefully acknowledge the financial support from the China National Key R&D Program under Grant No. 2019YFB1311600, the National Natural Science Foundation of China under Grant No. U1913213, and the grant for Distinguished Young Scholars of Shaanxi Province under Grand No. 2019JC-04

REFERENCE

1. HOWELL, L.L., MAGLEBY, S.P., OLSEN, B.M., *Handbook of Compliant Mechanisms*, John Wiley & Sons, 2013.
2. SMITH, S.T., *Flexures: elements of elastic mechanisms*, Crc Press, 2000.
3. FOLKERSMA, K.G.P., BOER, S.E., BROUWER, D.M., HERDER, J.L., SOEMERS, H.M.J.R., *A 2-dof large stroke flexure based positioning mechanism*, **4**: 36th Mechanisms and Robotics Conference, Parts A and B of International Design Engineering Technical Conferences and Computers and Information in Engineering Conference, pp. 221–228, 2012.
4. ZHAO, H., BI, S., YU, J., *A novel compliant linear-motion mechanism based on parasitic motion compensation*, Mechanism and Machine Theory, **50**, pp. 15–28, 2012.
5. CHOI, YEONG-jun, SREENIVASAN, S.V., CHOI, B.J., *Kinematic design of large displacement precision xy positioning stage by using cross strip flexure joints and over-constrained mechanism*, Mechanism and Machine Theory, **43**, *6*, pp. 724–737, 2008.
6. GROSSARD, M., MARTIN, J., HUARD, B., *Force-sensing actuator with a compliant flexure-type joint for a robotic manipulator*, Actuators, **4**, *4*, pp. 281–300, 2015.
7. HENEIN, S., SPANOUDAKIS, P., DROZ, S., MYKLEBUST, L.I., ONILLON, E., *Flexure pivot for aerospace mechanisms*, In 10th European Space Mechanisms and Tribology Symposium, San Sebastian, Spain, pp. 285–288, Citeseer, 2003.
8. ZHAO, H., BI, S., *Stiffness and stress characteristics of the generalized cross-spring pivot*, Mechanism and Machine Theory, **45**, *3*, pp. 378–391, 2010.
9. ZHAO, H., BI, S., *Accuracy characteristics of the generalized cross-spring pivot*, Mechanism and Machine Theory, **45**, *10*, pp. 1434–1448, 2010.
10. LIU, L., BI, S., YANG, Q., WANG, Y., *Design and experiment of generalized triple-cross-spring flexure pivots applied to the ultra-precision instruments*, Review of Scientific Instruments, **85**, *10*, 105102, 2014.
11. BI, S., ZHAO, H, YU, J., *Modeling of a Cartwheel Flexural Pivot*, ASME Journal of Mechanical Design, **131**, *6*, 2009.
12. PEI, X., YU, J., ZONG, G., BI, S., HU, Y., *A Novel Family of Leaf-Type Compliant Joints: Combination of Two Isosceles-Trapezoidal Flexural Pivots*, ASME Journal of Mechanisms and Robotics, **1**, *2*, 2009.
13. PEI, X., YU, J., ZONG, G., BI, S., *A Family of Butterfly Flexural Joints: Q-LITF Pivots*, ASME Journal of Mechanical Design, **134**, *12*, 2012.
14. MERRIAM, E.G., LUND, J.M., HOWELL, L.L., *Compound joints: Behavior and benefits of flexure arrays*, Precision Engineering, **45**, pp. 79–89, 2016.
15. JENSEN, B.D., HOWELL, L.L., *The modeling of cross-axis flexural pivots*, Mechanism and Machine Theory, **37**, *5*, pp. 461–476, 2002.
16. HOWELL, L.L., MIDHA, A., NORTON, T.W., *Evaluation of Equivalent Spring Stiffness for Use in a Pseudo-Rigid-Body Model of Large-Deflection Compliant Mechanisms*, ASME Journal of Mechanical Design, **118**, *1*, pp. 126–131, 1996.
17. WANG, Z., SUN, H., WANG, B., WANG, P., *Adaptive pseudo-rigid-body model for generalized cross-spring pivots under combined loads*, Advances in Mechanical Engineering, **12**, *12*, 1687814020966539, 2020.
18. ZHANG, A., CHEN, G., *A Comprehensive Elliptic Integral Solution to the Large Deflection Problems of Thin Beams in Compliant Mechanisms*, ASME Journal of Mechanisms and Robotics, **5**, *2*, 2013.
19. ZHANG, A., CHEN, G., JIA, J., *Large deflection modeling of cross-spring pivots based on comprehensive elliptic integral solution*, Journal of Mechanical Engineering, **50**, *11*, pp. 80–85, 2014.
20. AWTAR, S., SLOCUM, A.H., SEVINCER, E., *Characteristics of Beam-Based Flexure Modules*, ASME Journal of Mechanical Design, **129**, *6*, pp. 625–639, 2006.

21. MA, F., CHEN, G., *Modeling large planar deflections of flexible beams in compliant mechanisms using Chained Beam-Constraint-Model*, ASME Journal of Mechanisms and Robotics, **8**, *2*, 2015.
22. BILANCIA, P., BAGGETTA, M., HAO, G., BERSELLI, G., *A variable section beams based bi-bcm formulation for the kinetostatic analysis of cross-axis flexural pivots*, International Journal of Mechanical Sciences, 205:106587, 2021.
23. HOPKINS, J.B., PANAS, R.M., *Design of flexure-based precision transmission mechanisms using screw theory*, Precision Engineering, **37**, *2*, pp. 299–307, 2013.
24. HOPKINS, J.B., CULPEPPER, M.L., *Synthesis of multi-degree of freedom, parallel flexure system concepts via freedom and constraint topology (fact) c part i: Principles*, Precision Engineering, **34**, *2*, pp. 259–270, 2010.
25. HOPKINS, J.B., CULPEPPER, M.L., *Synthesis of multi-degree of freedom, parallel flexure system concepts via freedom and constraint topology (fact). part ii: Practice*, Precision Engineering, **34**, *2*, pp. 271–278, 2010.